THE ASTROPHYSICAL JOURNAL, 527:977–991, 1999 December 20
© 1999. The American Astronomical Society. All rights reserved. Printed in U.S.A.

TWO-TEMPERATURE CORONAL MODELS FROM *SOHO*/EIT OBSERVATIONS

J. ZHANG, S. M. WHITE, AND M. R. KUNDU
Department of Astronomy, University of Maryland, College Park, MD 20742
Received 1999 February 23; accepted 1999 August 5

ABSTRACT

We present a method for deriving a two–thermal-component approximation to the differential emission measure distribution of plasma in the Sun's corona in the temperature range to which the Extreme-Ultraviolet Imaging Telescope (EIT) on the *Solar and Heliospheric Observatory* (*SOHO*) spacecraft is sensitive. EIT takes high-resolution full-disk coronal images in three of its four optimized channels by observing emission lines of highly ionized Fe whose formation temperatures overlap and cover the range from 0.7 to 2.8 MK. It is straightforward to show that the traditional single-temperature models based on the ratio of a pair of EIT images at different wavelengths are not able adequately to represent the plasma contributing to all three wavelength ranges. In this paper, we develop a modified image-ratio method that results in a two–thermal-component model for the plasma producing the coronal emission observed by EIT. The products of this method are two temperature and two emission measure full-disk maps of the Sun's corona, with the full resolution of the EIT telescope, in two temperature regimes: one from 0.8 to 1.6 MK and the other from 1.6 to 2.6 MK. The two-component solutions are tested using a series of model differential emission measures (DEMs) from the CHIANTI atomic database package. This method appears to produce realistic results in all regions of the Sun's atmosphere with the exception of coronal holes, where very cool Si VII/Mg VII lines (<0.7 MK) contribute more to the EIT 284 Å image than the otherwise dominant hot Fe XV lines and result in unrealistically high temperatures for the hot component there. We demonstrate that while the raw EIT images are dominated by the spatial distribution of emission measure in the corona, the temperature maps often emphasize fine structure, which is less visible in the flux images. The emission measure of the hot component is always larger than that of the cool component. On the disk there appears to be a firm lower limit to the integrated column emission measure along any line of sight, including toward coronal holes. There is no overall correlation between temperature and emission measure.

Subject headings: Sun: atmosphere — Sun: corona — Sun: UV radiation

1. INTRODUCTION

The Extreme-Ultraviolet Imaging Telescope (EIT; Delaboudinière et al. 1995) on board the *Solar and Heliospheric Observatory* (*SOHO*) spacecraft provides full-disk images of the Sun with excellent spatial resolution (2.″6 pixels) in four EUV wavelength bands (Moses et al. 1997). Three of these bands are dominated by coronal lines chosen to cover a temperature range $0.7–2.8 \times 10^6$ K, which includes the bulk of the material in the solar corona (Raymond & Doyle 1981; Brosius et al. 1996). The EIT wavelength band selection is achieved through a multilayer coating technique that selects very narrow wavelength ranges, and thus the temperature response can be carefully selected. EIT data are available for most days since it started routine observations in 1996 January and thus represent a valuable resource for many types of solar study. Other EUV and UV telescopes, specifically, the Coronal Diagnostic Spectrograph (CDS) and the Solar Ultraviolet Measurement of Emitted Radiation (SUMER), both on *SOHO*) provide a powerful combination of imaging and spectral capability that is far superior to EIT for quantitative analysis of the temperature and emission measure distribution of plasma in the solar corona. However, the fields of view of these instruments are limited, and for a given region there is unlikely to be CDS or SUMER data unless that region was the target of a specific *SOHO* campaign involving these telescopes. On the other hand, chances are very good that excellent EIT data exist for any long-lived feature present on the Sun during the *SOHO* mission. Since 1996 January, EIT has taken synoptic sets of full-disk images in each of the four bandpasses a few times almost every day. Since 1996 December a deliberate policy of taking these four images nearly simultaneously (within 20 minutes) has been followed so that the precise alignment between images is preserved and temporal changes between images in different wavelengths are minimized. These synoptic data sets and many other sets of images with higher cadence yet smaller field of view constitute an extensive database that can be used for many purposes. For comparison with, e.g., radio data or other ground-based data sets, it is important to be able to exploit the quantitative information present in the EIT data to the fullest extent. This goal is the motivation for this paper.

The long history of EUV and soft X-ray spectroscopy of the solar corona has demonstrated that any finite volume of plasma within the corona displays a range of excitation states of abundant elements corresponding to a continuous distribution of temperatures throughout the emitting volume. In particular, since the Sun is essentially optically thin throughout this wavelength range, any image of the Sun necessarily integrates all the emission along the line of sight within each resolution element, and if structures with different temperatures are present at different heights in the corona, then they will all contribute to the observed emission and can produce a spectrum containing lines from a continuous range of temperatures. It would be desirable to have spatially resolved observations of many spectral lines covering a wide range of temperatures, such as CDS provides, in order to carry out an inversion to determine the distribution of emission measure with temperature (the

"differential emission measure" (DEM), e.g., Mason et al. 1997, McIntosh, Brown, & Judge 1998), but this will not be the case for an arbitrary target.

In analyzing observations that measure only a small number of parameters insufficient to characterize the full range of temperatures present in the solar atmosphere, we must necessarily make some approximations. The traditional approximation is to characterize the coronal emission as due to an isothermal plasma, i.e., characterized by just two parameters, a single temperature and emission measure. These can be determined by comparing two observations made with different wavelength bands, taking into account the spectral lines present in each bandpass and the response of the telescope as a function of wavelength. Essentially, the emission measure derived by such a technique represents the amount of plasma present within the temperature range to which the images are sensitive, while the temperature is an emission-measure–weighted temperature over the same range. This method has been extensively used in analyzing the observations of the Soft X-ray Telescope (SXT; Tsuneta et al. 1991) on the *Yohkoh* spacecraft. SXT uses filters to pick out different response, so that this method is called the "filter-ratio" method. SXT's filters are relatively broadband, i.e., they each include many spectral lines with different temperatures of formation. The temperature range to which SXT is primarily sensitive (i.e., where its response is strongest) is above 2×10^6 K, hotter than EIT's range. Specifically, if a significant amount of plasma at 3×10^6 K or hotter is present, then SXT is largely insensitive to plasma cooler than 2×10^6 K, and thus EIT complements SXT well. This filter-ratio method works well for bright soft X-ray loops in which a single hot component may be dominant. However, for general coronal regions the single-temperature assumption is not likely to be appropriate.

EIT is an imaging telescope divided into four quadrants, each with a different coating tuned to observe the Sun in specific EUV spectral lines. The standard suite of analysis routines for EIT data includes a routine to fit an isothermal model to any pair of EIT images, and this has been used for quantitative analysis (e.g., Aschwanden et al. 1998; Benz & Krucker 1999; Neupert et al. 1997). However, it is straightforward to show that use of a single pair of images to determine a temperature and emission measure provides a poor representation of the emission to which the three EIT coronal images are sensitive, and we demonstrate that in this paper. Nitta & Yaji (1997) have made the same point for SXT data, where sets of three-filter SXT images are usually only available in flare mode. One approach to quantitative analysis of three coronal images is to assume a universal functional form with three parameters for the DEM in the range of temperatures to which EIT is sensitive and to fit the three parameters on a pixel-by-pixel basis. This approach is being developed by Cook et al. (1998; they include the EIT transition-region image and fit a four-parameter function for the DEM). Here we investigate an alternative approach in which we approximate the DEM by two thermal components in the coronal temperature range to which EIT is sensitive, 0.7–2.8 MK. Such a representation requires four parameters, and thus we must specify a relationship between two of the parameters of the model. We show that a natural relationship exists and can be exploited. We also investigate the limitations of this approach, and in particular the difficulties caused because the EIT 284 Å bandpass include both hot and cool lines. In § 2, we briefly describe EIT observations and discuss the response of the different wavelength ranges in general terms. In § 3, we present the algorithm used to determine the parameters of the two–thermal-component model, and deal with some critical issues, including the non-unique nature of the solution. In § 4, we discuss the global properties of the temperature and emission measure distribution of the corona resulting from this approach. In § 5, we discuss anomalous two-temperature solutions found to occur in coronal holes. In the final section, we discuss the application and limitations of this method. We note that this method can trivially be extended to other similar EUV or soft X-ray data sets, such as the TRACE images in coronal bandpasses similar to those of EIT.

2. A SIMPLE GUIDE TO EIT DATA

In this section, we give a simple guide to the properties of EIT data necessary for understanding the development of the two-temperature models. More detailed descriptions of EIT data can be found in Delaboudinière et al. (1995) and Moses et al. (1997). EIT uses normal incidence multilayer optics to image the Sun on an EUV-sensitive 1024 × 1024 format charge coupled device (CCD) camera with a pixel size of 2.″6 and a field of view of 45′ × 45′. The optics are divided into four quadrants of matched multilayer pairs that are tuned to bandpasses centered at 171, 195, 284, and 304 Å, respectively. In Figure 1 we show the normalized temperature response curves of the three EIT coronal bandpasses. The temperature response curves show the expected flux in units of DN s^{-1} at a given temperature for a given emission measure (e.g., 10^{26} cm^{-5} here). The temperature responses are computed by convolving the instrumental response (effective collecting area) as a function of wave-

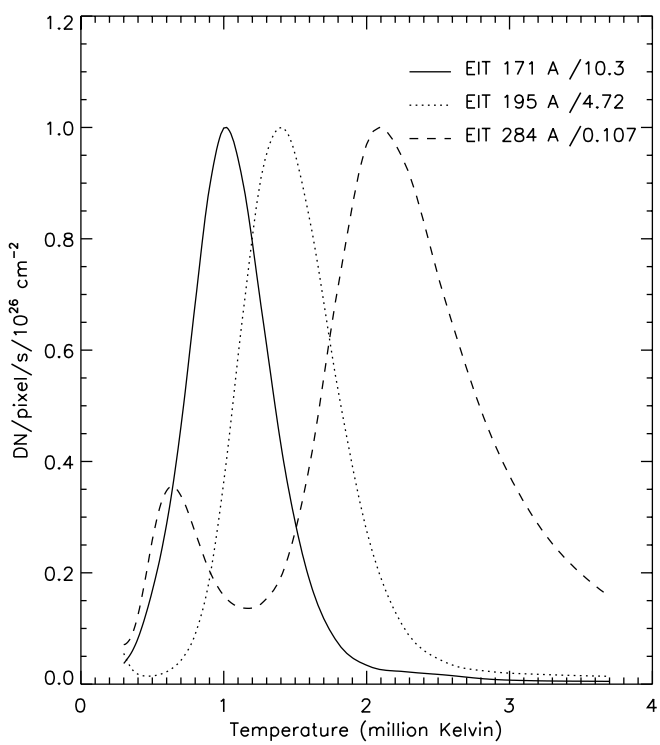

FIG. 1.—Normalized temperature response curves of EIT in the 171, 195, and 284 Å bandpasses for the "CLEAR" filter position. The normalization factors are 10.3, 4.72, and 0.107, respectively.

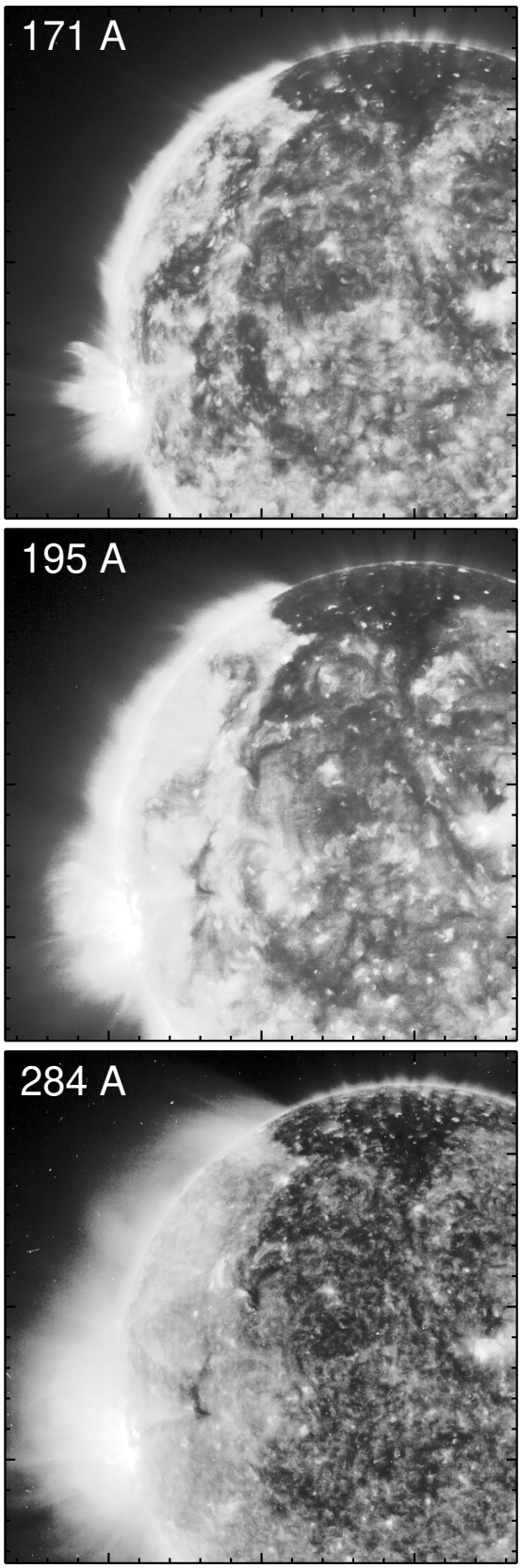

FIG. 2.—A set of EIT coronal images observed on 1996 July 27 at 171 Å (*top*), 195 Å (*middle*), and 284 Å (*bottom*) bandpasses. To exploit EIT's resolution, we show only a 640 × 640 pixel region of the full 1024 × 1024 pixel image, chosen to include a wide range of features. The Sun's north is to the top, and east is to the left. To emphasize fine-scale structure on the solar disk, the figures are displayed in the form of a histogram-equalized version of the logarithm of the raw images.

length (Delaboudinière et al. 1995) with theoretical solar X-ray spectra. In calculating the spectra, we use the CHIANTI atomic database (Dere et al. 1997), coronal abundances of Meyer (1985), and the ionization equilibrium calculations of Arnaud & Raymond (1992). In Figure 1 we show only the response curves at filter position "CLEAR." At the other two filter positions, Al + 1 and Al + 2, the curves are systematically lower, owing to the lower filter transmission, but have the same peak location and width. We also assume an electron density of 10^9 cm^{-3} in calculating the spectra used for Figure 1; the curves are relatively insensitive to electron density.

The response curve of EIT 171 Å has a single peak at temperature 1.0 MK with a FWHM of about 0.7 MK (from 0.7 to 1.4 MK), which is mainly contributed to by spectral lines of Fe IX at 171.07 Å and Fe X at 174.53 Å. (The shape of the peak for each bandpass is largely determined by the ionization abundance calculation for the dominant ion contributing to it.) The curve for EIT 195 Å has a peak at 1.4 MK with a FWHM about 0.8 MK (from 1.0 MK to 1.8 MK), which is mainly produced by spectral lines of Fe XII at 195.12 and 193.52 Å. The EIT 284 Å curve has two peaks. The primary peak is at temperature 2.1 MK with a FWHM 1.2 MK (from 1.6 to 2.8 MK), which is mainly due to a line of Fe XV at 284.16 Å. The secondary peak is at temperature 0.63 MK with a FWHM 0.51 MK (from 0.44 to 0.95 MK) and is produced by a number of spectral lines of Si VII and Mg VII ions that exist in this lower temperature range. We will show in § 5 that this blend of cool and hot lines in the EIT 284 Å bandpass results in ambiguous temperature solutions in coronal holes and other regions dominated by very cool plasma.

The fourth bandpass of EIT is the 304 Å bandpass dominated by the He II lines at 303.780, 303.785, and 303.786 Å formed at a transition-region temperature of about 0.08 MK. We do not include this bandpass in our analysis here because it is dominated by plasma much cooler than the coronal temperatures of the other bandpasses: the dominant temperature range to which the EIT 304 Å bandpass is sensitive does not overlap with the temperature ranges of the other EIT images, and therefore taking ratios of 304 Å images with coronal images is not useful. Radiative cooling is very rapid at 10^5 K, and DEMs determined from high-quality spectra always indicate a dearth of emission measure in the temperature range around 10^5 K, at least for long-lived features, so that to some extent the greater than 10^6 K and less than 10^5 K regions of the DEM are disconnected. We note however that the EIT 304 Å bandpass (see Delaboudinière et al. 1995) also includes a hot Si XI line (maximum ionization temperature at about 1.6 MK) and a number of Si VIII/Mg VIII lines (maximum ionization temperature at about 0.77 MK), which can contribute significantly in certain regions, and which result in considerable sensitivity of this band to plasma at coronal temperatures. On the disk up to 15% of observed EIT 304 Å flux comes from plasma at coronal temperatures, while coronal emission dominates the EIT 304 Å images in regions viewed above the solar limb, since the 10^5 K plasma that produces the 304 Å He II lines has a scale height much smaller than the scale height of the hotter coronal material. The method discussed here (and the method of Cook et al. 1998) can be used to remove the coronal contamination seen in EIT 304 Å images and thus produce a "clean" transition region image.

In Figure 2 we show a typical set of EIT coronal images: EIT 171 Å (*top*), EIT 195 Å (*middle*) and EIT 284 Å (*bottom*), which are taken at 22:19, 22:44, and 22:11 UT on 1996 July 27, respectively. In order to display EIT's resolution we show only a portion of the full-disk images, but the region shown includes a wide range of features: the coronal hole at the north pole, an active region on the east limb, a diffuse region above the northeast limb and quiet-Sun atmosphere dotted with bright points over much of the disk. These images have been flat-field corrected, background-subtracted, and normalized using the interactive data language (IDL) calibration routines in the standard EIT analysis package. The accuracy of spatial alignment between these images is about 2.″5, or one pixel, which is about the motion due to solar rotation at apparent disk center in the 30 minutes during which the images are taken. This accuracy is good enough for studying large-scale structures in the Sun's corona but may need further correction for studying fine structures such as coronal loops and bright points. We will process this set of images as an example to illustrate our two–thermal-component model.

3. TWO–THERMAL-COMPONENT MODELS

Here we derive the equations used to determine the parameters for a two-temperature model based on ratios of EUV images. First we summarize the traditional image-ratio (or filter-ratio) method based on a single-temperature assumption.

3.1. *Single-Temperature Models*

The observed flux in each bandpass is expressed as

$$f_i = \mathrm{EM} \times R_i(T) \,, \tag{1}$$

where f_i denotes the observed flux in the instrumental units of DN s^{-1}, EM denotes the emission measure or column density in units of cm^{-5}, R_i denotes the temperature response curve discussed in the previous section, and i denotes the bandpass, e.g., quadrant in EIT, filter in SXT, or spectral line in spectroscopic observations. In this paper bandpass 1 will denote EIT 171 Å, 2 denotes EIT 195 Å, and 3 denotes EIT 284 Å. From equation (1), for an isothermal plasma the ratio of the fluxes in two different bandpasses depends only on temperature, e.g., for the EIT 195 Å and 171 Å pair,

$$\frac{f_2}{f_1} = \frac{R_2(T)}{R_1(T)} \,. \tag{2}$$

The right-hand side of equation (2) is a calculated function of temperature, and the temperature of the plasma is then determined from the point where the flux ratio intersects the response ratio curve. The emission measure can then be derived immediately from

$$\mathrm{EM} = \frac{f_i}{R_i(T)} \,, \tag{3}$$

where i can be either 1 or 2. Note that the ratios of the temperature response functions (Fig. 1) are not monotonic: a given ratio may correspond to more than one temperature. However, it is found that over the temperature range to which a pair of adjacent bandpasses are sensitive, the response ratio curve is monotonic and the solution should be unique, e.g., the ratio curve is monotonic from 0.7 to 1.8 MK for the EIT 171 and 195 Å bandpasses. It is also necessary that the resulting temperature solution falls in the temperature range to which the bandpasses are sensitive.

This simple image-ratio method has been extensively used in analyzing SXT data. It is also the method available in the EIT software package in the routine EIT_TEMP, written by Jeff Newmark, which forms the starting-point for the method we discuss. EIT_TEMP forms a single-temperature model from pairs of EIT images; most observers seem to use the EIT 195 Å/171 Å ratio since the EIT 284 Å images have a lower flux level due to the relatively low reflectivity of the EIT 284 Å quadrant. However, we find that the synoptic EIT 284 Å images usually have enough signal for image-ratio analysis even at full resolution. Note that the exposure times of the EIT 284 Å synoptic images are usually at least 10 times longer than those of the EIT 171 and 195 Å images. A quiet-Sun pixel in an EIT 284 Å image typically has a photon count of about 80, and there are at least 30 photons for even the darkest pixels on the disk (a single 284 Å or 44 eV absorbed photon creates about 12 electron-hole pairs or 0.7 DN in a CCD pixel; one DN corresponds to 16.5 electron-hole pairs, and the average number of electron-hole pairs a photon of energy E produces is given by E/3.65 eV; see Delaboudinière et al. 1995).

The difficulty with the single-temperature approach is that one gets one answer from the 195 Å/171 Å ratio and a quite different answer from the 284 Å/195 Å ratio. To illustrate this difference, Figure 3 plots the 284 Å/195 Å ratio versus the 195 Å/171 Å ratio for each pixel inside 1.2 $R_\odot$. The pixels outside 1.2 $R_\odot$ are excluded in our analysis since their photon counts are usually close to the background noise level. In Figure 3 different regions in the ratio plane (denoted as A, B, C, and D) generally correspond to physically different regions of the solar atmosphere. Region A mostly contains pixels from the north and south polar coronal holes, region B (the most densely populated region of the ratio plane) mostly contains pixels in quiet-Sun areas, region C contains active-region pixels, and region D is populated by diffuse regions above the high-latitude limb. We emphasize that the single-temperature models for EIT data collapse this ratio plane into one dimension: specifically, the 195 Å/171 Å ratio uses only the information along the horizontal axis and completely ignores the information contained in the other dimension. Figure 3 demonstrates that such an approach will produce misleading results in many cases. The density of points in Figure 3 peaks at $f_2/f_1 = 0.50$ (i.e., 1.21 MK in a single-temperature model) and $f_3/f_2 = 0.025$ (1.76 MK in a single-temperature model), which corresponds to quiet regions of the solar atmosphere. As expected from the different response range of each bandpass shown in Figure 1, the temperature determined from the EIT 284 Å/195 Å ratio is always higher than that from the EIT 195 Å/171 Å ratio.

Also in Figure 3 we show the positions of calculated flux ratios for four coronal DEM models present in the current CHIANTI atomic database package, which correspond to so called active region DEM (labeled 1), bright quiet-Sun DEM (2), dark quiet-Sun DEM (3), and coronal hole DEM (4), respectively. These DEMs have been derived from a variety of sources of observed spectral line intensity. The active-region, bright quiet-Sun, and coronal hole DEMs were derived by Dere & Mason (1993) from the active-region spectra of Dupree et al. (1973), Vernazza & Reeves (1978), and Dere (1982); the quiet-Sun spectra of Dupree

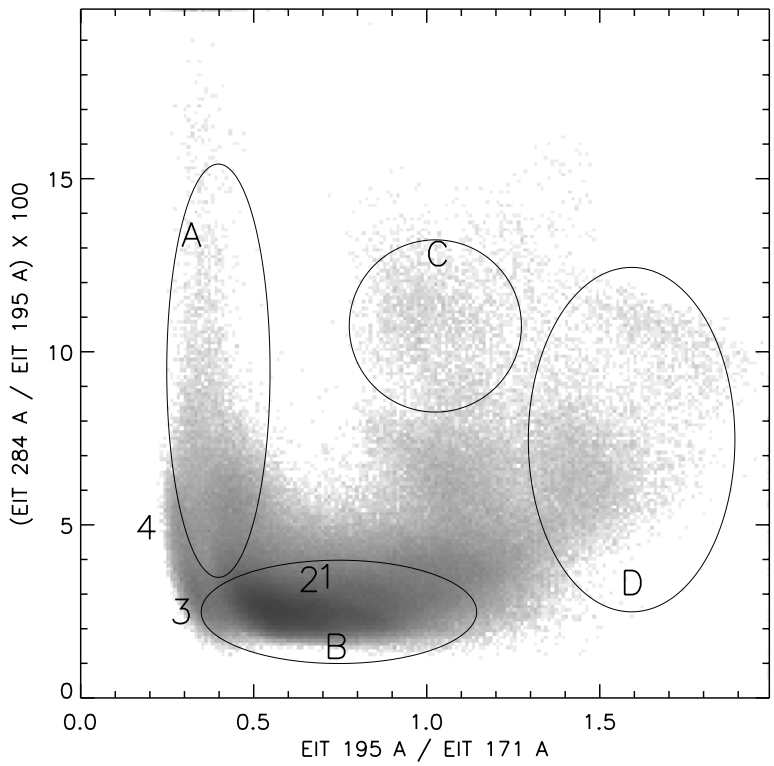

FIG. 3.—Plot of the EIT 284 Å/195 Å flux ratio (*y*-axis) vs. the EIT 195 Å/171 Å flux ratio (*x*-axis) for each pixel out to a radius of $1.2\,R_{\odot}$ in the EIT observations on 1996 July 27 shown in Figure 1. The regions within the ellipses A, B, C, and D correspond to coronal holes, quiet-Sun regions, active regions, and diffuse regions above the high-latitude limb, respectively. The number symbols 1, 2, 3 and 4 indicate the positions of calculated flux ratios for the active-region, bright quiet-Sun, dark quiet-Sun, and coronal hole DEMs from the CHIANTI package, respectively.

(1972), Heroux & Higgins (1977), and Vernazza & Reeves (1978); and the coronal hole spectra of Vernazza & Reeves (1978), respectively. The dark quiet-Sun DEM of Dere (CHIANTI package) comes from the spectral data of Dupree et al. (1973). As shown by their positions in the ratio plane, the bright quiet-Sun DEM represents well the average quiet Sun observed by EIT, while the active-region DEM actually represents a quiet-Sun region rather than an active region. The dark quiet-Sun DEM, whose flux ratio is located at the left edge of the distribution of observed ratios, represents the very dark quiet Sun, or even a coronal hole seen by EIT. The flux ratio corresponding to the coronal hole DEM lies in a region of the ratio plane that is never observed to be populated in actual EIT observations of the Sun and appears to be unphysical. We discuss these DEMs further in § 3.4.

Another way to test the validity of the single-temperature solutions is to produce model images in each bandpass from the derived temperature and emission measure using the known responses. It is always found that the single-temperature models fail to reproduce all three coronal images, e.g., the model based on the EIT 195 Å/171 Å ratio reproduces the EIT 171 and EIT 195 Å images well but not the EIT 284 Å image. The 284 Å flux produced by the single-temperature model based on the 195 Å/171 Å ratio contributes only about 2%–15% of the observed 284 Å flux (the percentage varies from region to region), while the reproduced flux at EIT 171 Å derived from the 284 Å/195 Å ratio model accounts for about 10%–40% of the observed 171 Å flux. This is hardly surprising, since we know that the corona is not isothermal, but it emphasizes the fact that we require a more sophisticated model to represent quantitatively the information present in the three EIT coronal images.

3.2. *Two-Temperature Models*

The simplest extension of a single-temperature model is to explore models composed of two thermal components, denoted cool (C) and hot (H). The observed flux in each bandpass is then expressed as follows:

$$f_1 = \mathrm{EM}_C \times R_1(T_C) + \mathrm{EM}_H \times R_1(T_H)\,, \quad (4)$$

$$f_2 = \mathrm{EM}_C \times R_2(T_C) + \mathrm{EM}_H \times R_2(T_H)\,, \quad (5)$$

$$f_3 = \mathrm{EM}_C \times R_3(T_C) + \mathrm{EM}_H \times R_3(T_H)\,. \quad (6)$$

In practice, we expect the 171 Å flux to be dominated by the cool component, and the 284 Å flux to be dominated by the hot component. The 195 Å flux will receive contributions from each thermal component: at a very crude level one can think of the two-temperature analysis as determining the relative fractions of the observed 195 Å flux produced by the hot and cool components.

Both EM_H and EM_C can be eliminated by combining these three expressions, resulting in an expression (analogous to eq. [2]) that contains only the temperature responses and the observed fluxes:

$$f_1 \times [R_3(T_C) \times R_2(T_H) - R_2(T_C) \times R_3(T_H)] + f_2 \times [R_1(T_C) \times R_3(T_H) - R_3(T_C) \times R_1(T_H)] + f_3 \times [R_2(T_C) \times R_1(T_H) - R_1(T_C) \times R_2(T_H)] = 0\,. \quad (7)$$

This equation can be solved in conjunction with an additional constraint, discussed below, to determine the tem-

peratures T_C and T_H. Once the temperatures are determined, we can derive the emission measures from

$$E_C = \frac{f_1 \times R_2(T_H) - f_2 \times R_1(T_H)}{R_1(T_C) \times R_2(T_H) - R_2(T_C) \times R_1(T_H)} \quad (8)$$

and

$$E_H = \frac{f_1 \times R_2(T_C) - f_2 \times R_1(T_C)}{R_1(T_H) \times R_2(T_C) - R_2(T_H) \times R_1(T_C)} . \quad (9)$$

3.3. *Additional Constraint*

A two-component model has four free parameters to be determined (two temperatures and two emission measures). Since we measure only three quantities at each pixel, we must impose an additional constraint. Since EIT is sensitive only to material in a relatively small range of temperatures because of the nature of the EIT bandpasses, whereas there is essentially no restriction on the range of emission measure to which EIT is sensitive, it is natural to look for a constraint on the temperatures of the two components, and in particular on their ratio

$$\alpha = \frac{T_H}{T_C} , \quad (10)$$

where T_H is the temperature of the hot component and T_C is the temperature of the cool component. Initially we investigated fixing this ratio while allowing the actual values of T_C and T_H to vary from cooler to hotter values, thereby allowing the solution to represent the full range of temperatures covered by the coronal bandpasses (Fig. 1). As an example, since the range of temperatures covers a factor of about four (0.7–2.8 MK), the choice $\alpha = \sqrt{4}$ would allow considerable freedom in T_C and T_H while maintaining a good separation of the components.

Once a value of α (or an algorithm for determining it) is imposed, it can be used to substitute αT_C for T_H in equation (7), making it an equation that can be solved for the sole remaining variable, T_C, for any given set of observed fluxes f_1, f_2, and f_3. Note that R_1, R_2, and R_3 are temperature response curves calculated from the bandpass shapes and model spectra as discussed in the previous section.

Solving equation (7) amounts to finding the zero of a function, which we refer to as the "solution curve." We also require that the solution should lie in the range of temperatures to which the EIT bandpasses are sensitive. In Figure 4 we show the solution curves for a series of temperature ratios and a representative set of flux values: the curves 1, 2, 3, 4, 5, and 6 correspond to the temperature ratios $\alpha = 1.3$, 1.5, 1.7, 1.9, 2.1, and 2.3, respectively. The set of input fluxes ($f_1 = 96.9$ DN s^{-1}, $f_2 = 61.5$ DN s^{-1}, and $f_3 = 1.90$ DN s^{-1}) are calculated from the CHIANTI bright quiet-Sun DEM, which represents the average quiet Sun observed by EIT.

In Figure 4 no solution (i.e., crossing of zero by the curve) exists for curves 1 and 2 (small values of α) in the desired temperature range. Two close solutions are found for curve 3 (at $T_C = 1.15$ MK), and higher values of α produce two well-separated solutions: $T_C = 0.96$ and 1.27 MK for curve 4, $T_C = 0.87$ and 1.27 MK for curve 5, and $T_C = 0.78$ and 1.27 MK for curve 6. The important result is that solutions do not exist for arbitrary values of the two temperatures.

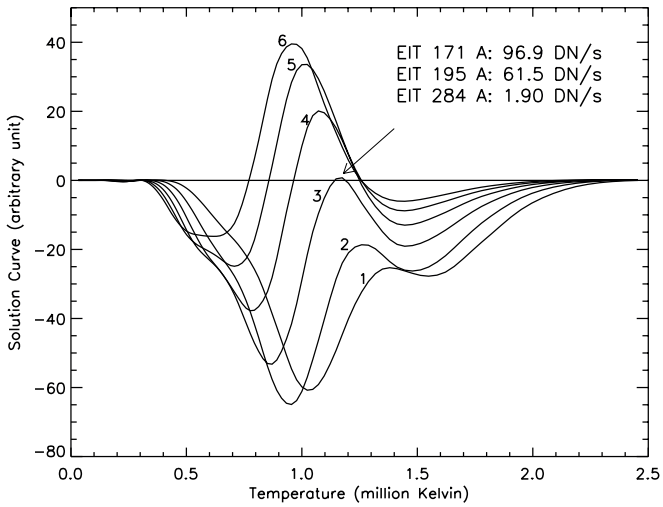

FIG. 4.—Changes in the "solution curves" (the left-hand side of eq. [7]) as a function of the temperature ratio T_H/T_C for a given set of EIT fluxes. The input EIT fluxes (*upper right-hand corner*) are calculated using the CHIANTI bright quiet-Sun model DEM. The curves labelled 1, 2, 3, 4, 5, and 6 correspond to temperature ratios 1.3, 1.5, 1.7, 1.9, 2.1, and 2.3, respectively. A solution for the temperature of the cool component is found wherever the curve has a zero-crossing point.

We find this to be a general result: for all observed pairs of flux ratios found in Figure 3, there is a lower limit to the ratio α of the two temperatures for which solutions of equation (7) exist. This lower limit varies considerably from place to place in the solar atmosphere: in region A of Figure 3 (coronal holes), it is over 1.9; in region B it is from 1.5 to 1.7; in region C it varies from 1.7 to 1.9; and in region D it is below 1.6. The fact that a minimum value of α exists for all observed sets of f_1, f_2, and f_3 offers us an alternative constraint to the assumption of constant-α suggested above: at each pixel we choose the minimum α for which a solution exists. This is the constraint we use in the algorithm we discuss in the remainder of the paper. Note that Nitta & Yaji (1997) simply fix the cool temperature value in their two-temperature model for analyzing three-filter SXT observations, where the range of temperatures capable of contributing to the observed flux is much larger than is the case for EIT.

3.4. *Uniqueness of the Solutions and Justifications*

The minimum T_H/T_C ratio has been added to the three observational constraints in order to determine the four parameters needed to describe a two–thermal-component model. However, the selection of the temperature ratio is still somewhat arbitrary since any value above the minimum value for which a solution exists is a mathematically valid solution. Thus, on what physical grounds do we justify our particular choice? Effectively, the minimum temperature ratio requirement produces a solution in which the total emission measure is close the minimum possible EM that can reproduce the observed fluxes. A simple way to think about this is to adopt the crude assumption that the observed flux from the EIT 171 Å bandpass is purely provided by the cool component and the EIT 284 Å flux is purely from the hot component, while the EIT 195 Å flux is from both. This assumption is reasonable since the temperature response of EIT 171 Å has little overlap with that

of EIT 284 Å (Fig. 1). Since $f_1 \sim \mathrm{EM}_C R_1(T_C)$, the closer T_C is to the peak of the response $R_1(T)$ of the EIT 171 Å bandpass, the smaller EM_C will be; equally the closer T_H is to the peak of the EIT 284 Å response, the smaller EM_H will be. If the temperatures of the two components are so close that their ratio is small, they will both lie near the peak of the EIT 195 Å response and thus well away from the peaks of both EIT 171 Å and 284 Å responses. As a result, the solutions for the emission measures in the two components must necessarily be high, and the combined contribution of the cool and hot components to the EIT 195 Å bandpass would then always exceed the observed flux. This is the reason why α must exceed some minimum at each pixel in order for a two-temperature solution to exist. Similarly, if the temperature ratio is very large, then at least one of the resulting temperatures must always lie well away from the peak responses of the three bandpasses and the emission measures required to reproduce the images will be unnecessarily large.

We have carried out a simple simulation to further illustrate this analysis. In Figure 5, we plot a set of two-temperature solutions (emission measure versus temperature) calculated with seven different temperature ratios (ratios 1.7, 1.9, 2.1, 2.3, 2.5, 2.7, and 2.9, denoted by the number labels 3, 4, 5, 6, 7, 8, and 9, respectively). Note that the lower sequence of ratio 1.3 and 1.5 do not give rise to any solution. The minimum-ratio solution is denoted as a pair of filled circles in Figure 5. For each temperature ratio above the minimum possible value there are two possible solutions (see Fig. 4), and these are plotted to the right and left of the minimum-ratio solution as triangles and diamonds, respectively. The minimum ratio in this case is just below 1.7, i.e., it lies between the diamond and the triangle labeled 3 on the figure. Figure 5 shows how in general the required temperature and emission measure vary as α increases above the minimum value. The solutions trace out a quasi U-shape that is almost the inverse of the response curve, since as you move away from the temperatures of the peak responses in Figure 1 more EM is required to produce the same flux. In Figure 5, the solid curve indicates the model DEM (CHIANTI bright quiet-Sun DEM) used to calculate the fluxes (to put the DEM curve on a plot where the Y axis has units of EM, we use EM(0.3) instead, which is derived by integrating DEM from $\log T - 0.15$ to $\log T + 0.15$ for any given temperature T: see the discussion by Griffiths & Jordan 1998). We can then estimate the "best" two-temperature representation of the DEM by integrating the DEM over the temperature range to which EIT is sensitive and splitting it into two temperature regimes: one is from 0.7 MK up to some division temperature, and the other is from the division temperature up to 2.8 MK. The division temperature is chosen to lie between the two solution temperatures and should be close to the peak response temperature of EIT 195 Å. For simplicity, we choose the division temperature such that it and the temperatures from the minimum-ratio solutions have the same geometric relationship as the peak response temperatures of the EIT 195, 171, and 284 Å bandpasses, which in this example is 1.41 MK (indicated by the *vertical dotted line*). The expected temperatures are then averages weighted by the differential emission measure in each regime. These values are shown as a pair of asterisks in Figure 5 and lie quite close to the solutions determined using the minimum temperature ratio algorithm. Solutions determined

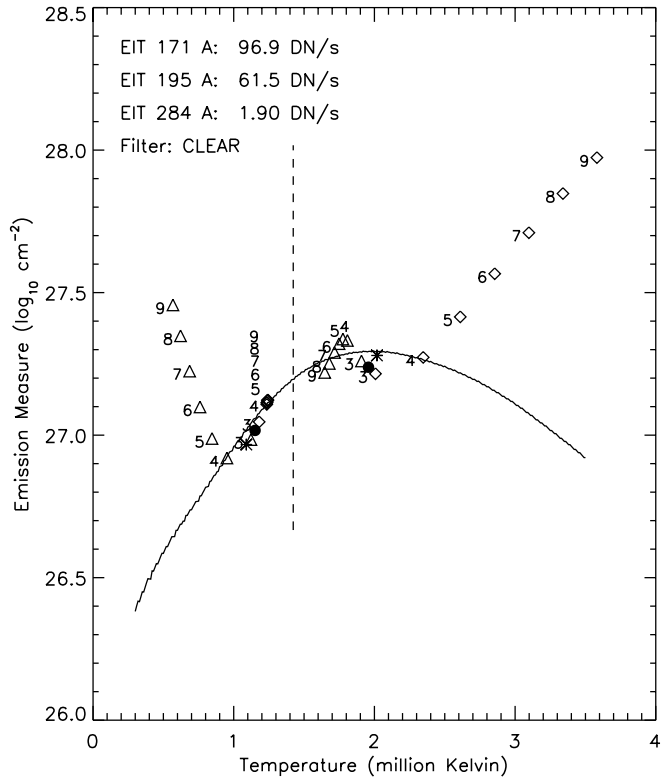

FIG. 5.—Comparison of temperatures and emission measures (a pair of symbols) calculated from the two–thermal-component model with that predicted from a model differential emission measure distribution (i.e., average quiet Sun). The solid curve shows EM(0.3) (i.e., the model DEM integrated over bins of width 0.3 in the logarithm of the temperature; see text). The fluxes for each EIT bandpass calculated from this DEM are shown in the upper left-hand corner. Filled circles indicate the solution corresponding to the minimum temperature ratio for which a solution exists, while the asterisks show the solution expected by integration of the model DEM. The numbers 3, 4, 5, 6, 7, 8, and 9 correspond to temperature ratios 1.7, 1.9, 2.1, 2.3, 2.5, 2.7, and 2.9, at each of which a pair of solutions is found (the two points of intersection between 0.7 and 1.7 MK for each curve in Fig. 4). Triangles denote models using the cooler solution for T_C in Fig. 4, while diamonds denote the hotter solution. Note that many of the diamonds for the cool component lie nearly on top of one another. The vertical dotted line indicates the position of the division temperature that is chosen to split the DEM into two components.

assuming large temperature ratios lie well away from the DEM-weighted values and away from EM(0.3) curve.

We have carried out this test for a variety of smooth model DEMs, including the four CHIANTI DEMs discussed in previous section. It is always found that the solutions at the condition of minimum temperature ratio are better than other solutions with higher temperature ratio, since these solutions lie closer to the DEM-predicted solutions and also closer to the EM(0.3) curve. In Figure 6 we plot the solutions of minimum temperature ratio (denoted by a pair of *filled circles*) against the EM(0.3) curves (*solid line*) for CHIANTI active-region, bright quiet-Sun, dark quiet-Sun, and coronal hole DEMs in Figures 6*a*–6*d*, respectively. In the same figure, we have also plotted the predicted two-component solutions (*asterisks*), which are calculated by partitioning the DEM into two temperature regimes using the method described in the last paragraph. For a further comparison, we also plot the traditional isothermal solutions determined from the EIT 195 and 171 Å pair (*diamond*) and by the EIT 284 Å and 195 Å pair (*triangle*). For the active-region and bright quiet-Sun

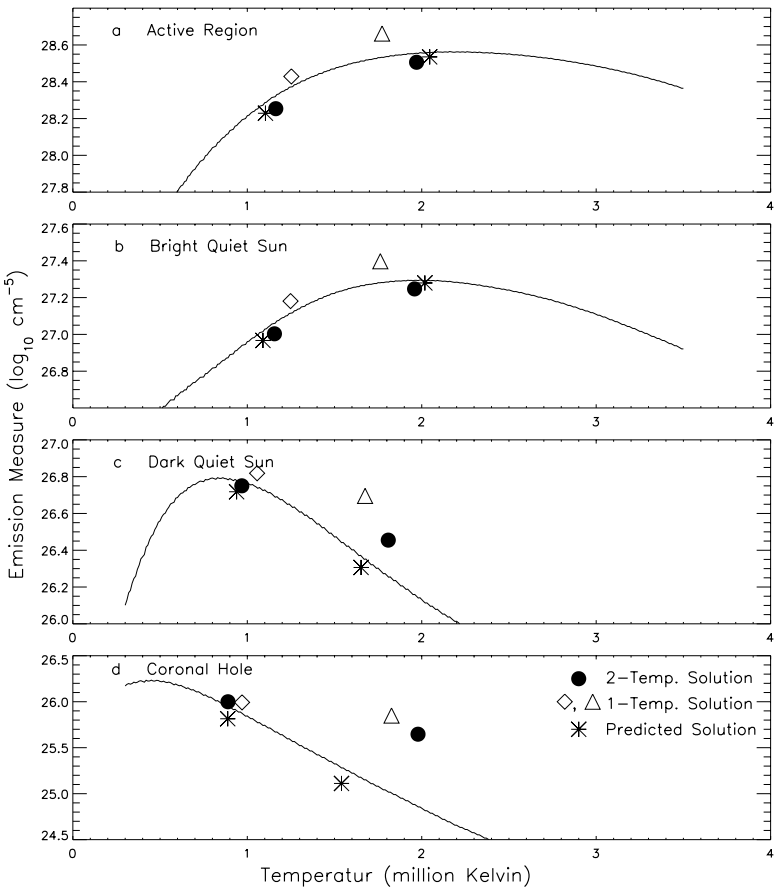

FIG. 6.—Comparison of the temperature and emission measure solutions (*pair of filled circles*) from the two–thermal-component model under the minimum temperature ratio assumption with predicted two-component solutions (*asterisks*) for four different CHIANTI model DEMs (shown by the *solid curves* that plot EM[0.3]). We also plot the solutions from the traditional isothermal model applied to the EIT 195 Å/171 Å ratio (*diamond*) and the EIT 284 Å/195 Å ratio (*triangle*). From top to bottom, the input model DEM represents the active-region DEM (*a*), bright quiet-Sun DEM (*b*), dark quiet-Sun DEM (*c*), and coronal hole DEM (*d*), respectively.

DEMs, our two-component solutions match the predicted solutions very well, while for the dark quiet-Sun and coronal hole DEMs the cool component solutions are as predicted whereas the hot component solutions deviate significantly from the predicted solution: both the temperature and emission measure are too high. The reason for the deviation is the presence of cool material below 1 MK in these DEMs, which contaminates the EIT 284 Å image through the Si VII and Mg VII lines in the bandpass. This issue will be discussed further in § 5. Comparing the traditional isothermal solutions with our two-component solution, it is found that the isothermal solutions from the EIT 195 Å and 171 Å pair always give rise to a higher temperature and higher emission measure than that of the cool component of our solution, while the isothermal solutions from the EIT 284 Å and 195 Å pair give rise to a lower temperature and higher emission measure than that of the hot component of our solution. These results are understandable since the EIT 195 Å flux must be accounted for completely in each of the two isothermal models, whereas it is divided between the two components in our models.

In addition, we have also carried out tests for extreme examples of DEMs that are not smooth. For a single-temperature DEM, we find that one component of the two-temperature solution for the model fluxes is close to the input temperature and emission measure, and the other component gives a much lower emission measure but a similar temperature (i.e., a very small temperature ratio). Since the input model has only two free parameters, our three-parameter model does quite a good job of reproducing it. The case of a model DEM containing two isothermal components is more complicated. Here the input model has four free parameters, so some information is lost when we create the three model fluxes. When the two components lie at temperatures between the peak responses of the 171 Å and 284 Å images, the solutions are usually in good agreement with the original values. However, if the two model temperatures are such that one of them dominates the flux in the 195 Å image (e.g., $T_C = 1.3 \times 10^6$ K and $T_H > 2.5 \times 10^6$ K, in which case the cool component dominates), the model retrieves the temperature and emission measure of the component dominating the 195 Å flux quite well, but the temperature of the other component is not correct. This is a case where the actual temperature ratio in the input model is much larger than the minimum temperature ratio permitted by the fluxes. In some sense, the two-temperature analysis works better (paradoxically) when the DEM is smooth.

In summary, our two-temperature-component solutions derived with the minimum temperature ratio assumption represent the integrated plasma along any line of sight with two isothermal components. When the plasma has a smooth DEM distribution, our solutions adequately reproduce the average temperatures and summed emission mea-

sures in the two regimes of the DEM to which EIT is sensitive (0.7–2.8 MK), which are partitioned at a temperature close to the peak temperature of the EIT 195 Å bandpass (1.4 MK). We emphasize here that the emission measure of our solution is not the emission measure of the coronal plasma at a specific temperature, but rather an integrated emission measure of the DEM over a temperature range, e.g., $\approx$0.7–1.4 MK for the cool component. Similarly, the temperature in our solution is not the temperature of a specific isothermal plasma in the corona, but rather an average temperature weighted by the DEM over the appropriate temperature range. The two thermal components of the model are not "real" in the sense that the Sun's plasma in each pixel does not actually consist of two components with the derived properties: the two-component model is a means for representing the DEM present in each pixel in a physically intuitive manner.

3.5. *Error Estimation*

Here we discuss possible sources of error in the two–thermal-component solutions, which result from photon statistical errors and uncertainties in instrumental calibration. Note that the abundance uncertainty of Fe has no net effect in our estimation of temperature and relative emission measure, since the three coronal images are all dominated by Fe lines. Also note that the theoretical solar EUV spectra used for modeling have been calculated assuming thermal equilibrium and ionization balance, which may not be appropriate in all circumstances. However, we expect that the deviation from those assumptions will be small in the coronal temperature range for features not varying rapidly in time.

Statistical error is caused by photon Poisson noise, i.e., for N photons detected by the CCD the intrinsic signal-to-noise ratio is of order $\sqrt{N}$. The high sensitivity and the optimized exposure times of EIT for each bandpass usually yield sufficient photons for uncertainties to remain low, e.g., a typical quiet-Sun region on the disk produces 80 photons per pixel in EIT 284 Å images and much larger photon counts per pixel in the EIT 171 Å and 195 Å images. We estimate that the uncertainty due to photon noise in the emission measure of the cool component resulting from this method, which is mainly determined by the EIT 171 and 195 Å images, is typically about 2%, 10%, and 15% for active regions, quiet Sun, and coronal holes, respectively. The corresponding uncertainties in the solution for the temperature of the cool component are about 0.01, 0.04, and 0.06 MK, respectively (uncertainties in the temperature solutions are small owing to the temperature sensitivity of each bandpass, see Fig. 1). For the hot component, which is mainly determined by the EIT 284 and 195 Å images, the typical uncertainty in the derived emission measure due to photon noise is about 4%, 20%, and 30% for active regions, quiet Sun and coronal holes, respectively, while the corresponding uncertainties in the temperature of the hot component are about 0.02, 0.10, and 0.20 MK, respectively. Note that it would be computationally expensive to solve equation (7) exactly at each pixel, so in view of the uncertainty due to photon noise the IDL code as implemented uses a regular grid of possible temperatures and temperature ratios chosen so that the error caused by approximating the solution to equation (7) in this way is smaller than likely sources of uncertainty due to photon noise, permitting the calculation to be carried out efficiently. We have tested our code by comparing the model images calculated from the temperature and emission measure solutions with the observed images. It is found that the deviation of the model images from the observed images is less than 3% in the EIT 171 and 195 Å images and less than 10% in the EIT 284 Å image.

Another source of uncertainty that must be addressed is produced by temporal variability: any transient brightenings with timescales shorter than the typical 30 minute interval over which the synoptic EIT images are taken will result in features appearing to be different in the different bandpasses. Such features will usually be compact features and can generally be recognized in the data directly.

This method, in common with any attempt to use EIT images quantitatively, relies on the response and throughput for each EIT bandpass being known. The absolute values of the temperature and emission measure for the two components (which, it should always be recalled, are a representation of a continuous DEM within the temperature range to which EIT is sensitive) depend critically on instrumental calibration. Moses et al. (1997) have discussed instrument calibration issues in detail. The overall instrument throughput, which is monitored by the total flux in a full field image for each bandpass, is mainly degraded by CCD surface contamination and the reduction of CCD efficiency due to EUV-induced damage. At present, it is assumed that the 284 and 304 Å images suffer the same degradation in throughput, which is measured from the time variation of the flux in the 304 Å image, which has higher count rates, and in addition it is assumed that the 171 and 195 Å images suffer the same degradation in throughput. Bake-outs are carried out routinely to maintain a high CCD efficiency, and CCD flat-field calibrations are measured. It is recognized that the flat field can be distorted by strong local solar features, which degrade the CCD more severely than weak features. An additional complication is the fact that over the lifetime of the mission, the pixels that are always illuminated by the solar disk have suffered far more degradation than those that are always outside the limb: disk pixels are up to 50% less efficient than at the start of the mission, while off-limb pixels have degraded 5% at most. The annulus of pixels over which the limb moves as *SOHO*'s orbit takes it nearer to and further from the Sun have suffered varying degrees of degradation. The EIT calibration software contains options to try to deal with these problems (J. Newmark, 1999, private communication. We have included these options in processing the raw data). Determination of the responses of the different bandpasses and correction for flat-field distortion is an ongoing process being carried out by the EIT consortium (D. Moses, 1999, private communication) in conjunction with calibration data from other instruments. An accuracy of 5% is in principle achievable. In common with EIT_TEMP, our routine merely needs to have the response as a function of temperature specified, and if this changes as the calibration is better understood, then the relevant data can easily be corrected. Usually, the early observations and those taken immediately following bake-outs have less calibration uncertainty and thus can be used more safely. A systematic uncertainty of up to 50% or more for the current EIT calibration is apparently possible.

In summary, the EIT synoptic images have noise levels low enough for the determination of two-component thermal models with quite small formal uncertainties due

purely to photon noise. Much larger systematic uncertainty is associated with the instrumental calibration. Until the calibration is better understood, the temperatures and emission measures determined from this method will be more valuable for those studies in which trends in the relative temperature and emission measure are significant. The uncertainty in instrument calibration affects the determination of absolute temperature to a limited extent because of the uncertainty in the relative response of the different bandpasses, but this is much smaller than the absolute uncertainty in each response individually: thus in absolute terms the temperatures may be in error by as little as 0.2 MK as a result of calibration uncertainty, while emission measures are uncertain by a factor of 2.

4. TEMPERATURE AND EMISSION MEASURE DISTRIBUTIONS IN THE SOLAR CORONA

We have developed an IDL routine based on EIT_TEMP that produces two-temperature models from EIT data using the algorithm introduced above. For each set of EIT images in the three coronal bandpasses, the program calculates images of T_C, T_H, EM_C, and EM_H with the same resolution as the original images. Figure 7 shows the results of applying this analysis to the images of Figure 2. The emission measure maps are very similar in appearance to the observed 171 and 284 Å flux images while the temperature maps can be very different. Since the emission measure may vary by 3 orders of magnitude from region to

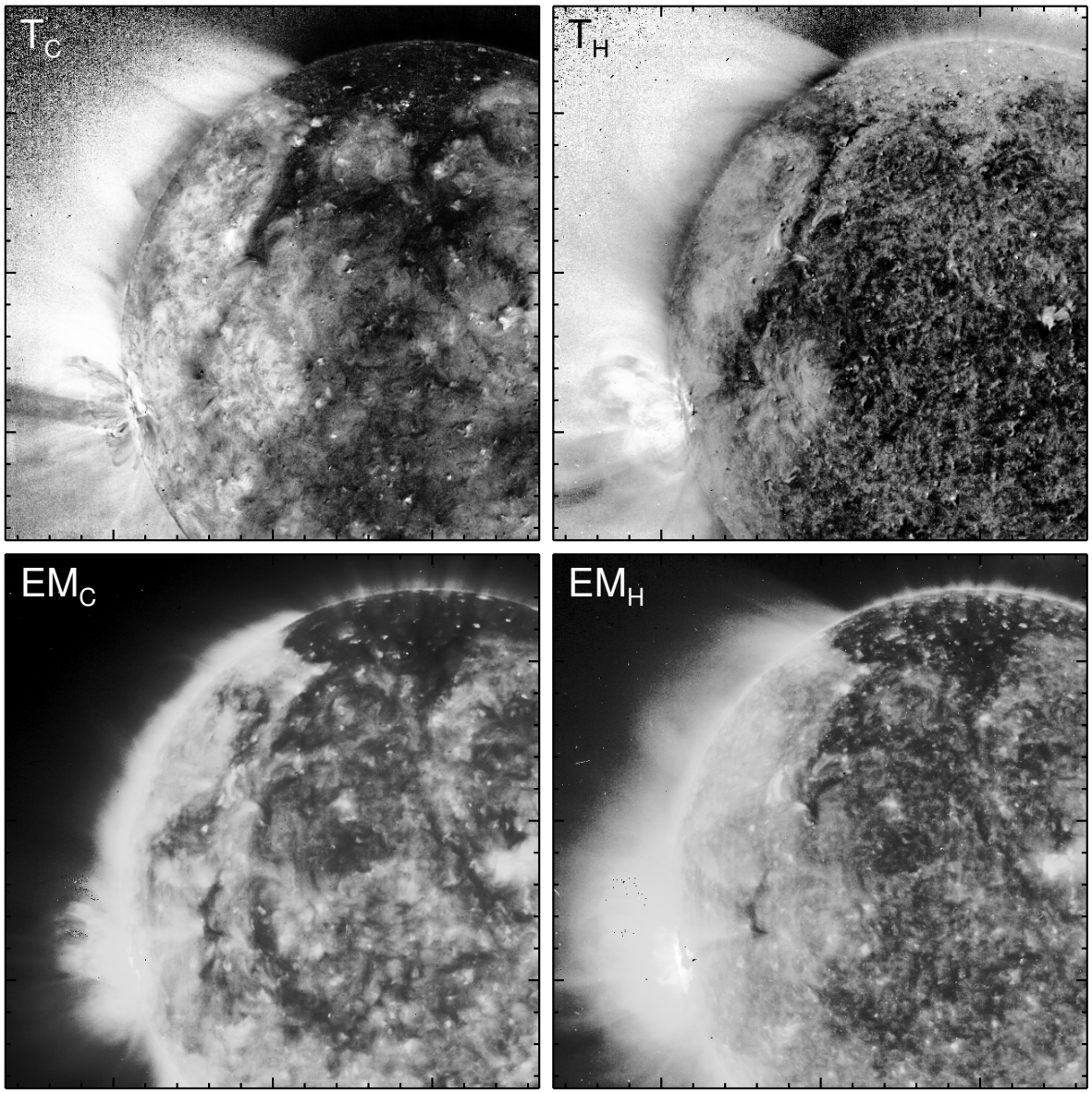

FIG. 7.—Maps of the temperatures of the cool (*left*) and hot (*right*) components (*top panels*) and the corresponding emission measure maps (*bottom panels*) resulting from the 1996 July 27 EIT observations derived from our two–thermal-component model. The temperature is displayed in histogram-equalized form over the range from 0.7 to 1.7 MK for the cool component (*left*) and 1.6 to 2.6 MK for the hot component (*right*). The emission measure maps use histogram equalization of the logarithm of the emission measure, covering the range from $10^{25.6}$ to $10^{29.0}$ cm^{-5} for the cool component and $10^{25.7}$ to $10^{29.3}$ cm^{-5} for the hot component. Note that the EM_C map is very similar in appearance to the 171 Å map in Fig. 2, and the EM_H map is very similar to the 284 Å image, while the temperature maps do not resemble any of the original images in detail.

region while the temperature is limited to a narrow range, the observed flux images are dominated by the variation of plasma emission measure. The temperature maps obtained from the image-ratio method show subtle features not readily evident in the flux images.

As an example, the boundary between the north polar coronal hole and the diffuse emission above the north-east limb is much sharper in the temperature maps than in the emission measure maps because of the low fluxes there. We also clearly see a jetlike structure above the active region on the east limb in the map of the temperature of the cool component, but not in any of the other three maps. The jetlike structure is quite thick and extends beyond the EIT field of view. In the cool temperature map we also see a few large and thin cool loops embedded in the relatively hot diffuse plasma above the north-east limb. Both temperature maps show a temperature gradient in the diffuse emission above the north-east limb, with temperature increasing outward as expected in a gravitationally stratified atmosphere. In the polar regions enhancements of polar plumes are prominent in the emission measure maps (and the original images) but not at all in the temperature maps: their temperature is almost identical to that of the surrounding atmosphere. For the diffuse component on the disk, enhancements of emission measure are not always accompanied by the enhancements in temperature one might expect in more strongly heated regions. However, for the compact bright points dotted about in quiet-Sun regions of the atmosphere, both the emission measure and the temperature are well above the levels typical of the background diffuse component. The difference between structures in the temperature and emission measure maps is potentially very revealing (e.g., see the discussion by Tsuneta 1999), since the temperature maps presumably more directly reflect the immediate heating and cooling history of a region, while the emission measure maps also show the effects of evaporation in response to coronal heating events.

In Figure 8 we show the distributions of the values of the cool temperature T_C (Fig. 8*a*), hot temperature T_H (Fig. 8*b*), cool-component emission measure EM_C (Fig. 8*c*) and hot-component emission measure EM_H (Fig. 8*d*). The solid curves show the distribution for pixels inside 1.0 $R_\odot$, while the dotted curve also includes pixels inside 1.2 $R_\odot$. T_C varies from 0.9 to 1.6 MK, with most pixels in the range 1.05–1.3 MK. T_H varies from 1.6 to 2.6 MK, with most pixels in the range 1.8 to 2.1 MK. It is noticeable that the range of values of T_C corresponds well to the EIT 171 Å temperature sensitivity range while the range of values of T_H corresponds well with the EIT 284 Å temperature sensitivity range. This is a natural consequence of the responses plotted in Figure 1 and illustrates the fact that we are representing the DEM in the temperature range to which EIT is sensitive by two isothermal components that are necessarily weighted according to the peak responses of the three EIT band-

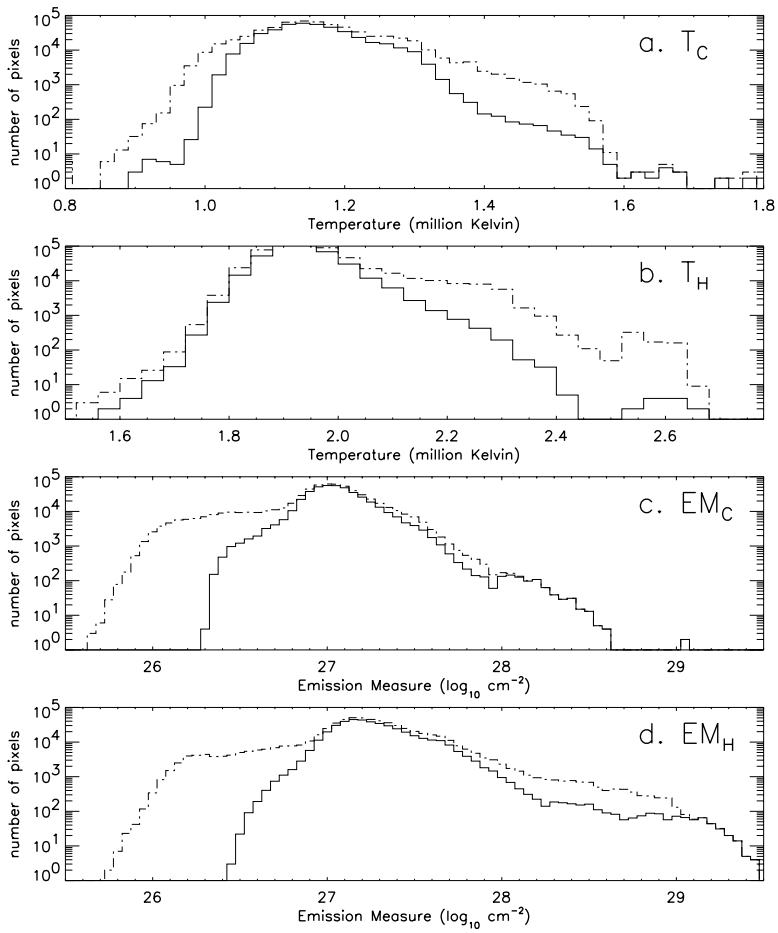

FIG. 8.—Histogram distribution of the temperature of the cool component (*a*), the temperature of the hot component (*b*), the emission measure of the cool component (*c*), and the emission measure of the hot component (*d*) of the solution in two–thermal-component model for observation on 1996 July 27. The solid curves show distributions for pixels inside 1.0 $R_\odot$, while the dotted curve includes all pixels inside 1.2 $R_\odot$.

passes. (On the other hand, the ratio T_H/T_C varies quite widely, from 1.4 up to 2.0, with a tail of values extending up to 2.2. The most common T_H/T_C ratio is close to 1.6.) We point out again that the actual values of T_C and T_H cannot be taken too seriously. However, we can expect that trends in T_C and T_H are significant. Typical values of T_C in active regions, diffuse regions above the limb, quiet-Sun regions, and coronal holes are 1.3, 1.4, 1.15, and 1.0 MK, respectively; typical values of T_H are 2.3, 2.1, 1.9, and 2.0 MK, respectively.

The typical emission measures of active regions, quiet-Sun regions and coronal holes are $EM_C = 1 \times 10^{28}$ and $EM_H = 7 \times 10^{28}$, $EM_C = 1 \times 10^{27}$ and $EM_H = 1 \times 10^{27}$, and $EM_C = 5 \times 10^{26}$ cm^{-5} and $EM_H = 6 \times 10^{26}$ cm^{-5}, respectively. It is important to note that in all regions the emission measure of the hot component is at least as large as, and usually larger than, the emission measure of the cool component. Since the single-temperature models derived from the EIT 195 Å/171 Å ratio that are commonly used are largely sensitive only to the cool component, they may be ignoring more than half of the emission measure to which EIT is sensitive.

An interesting feature of the emission measure distributions is the presence of a sharp lower cutoff in the emission measure of the corona projected against the solar disk. From the solid curves in Figures 8*c* and 8*d*, we clearly see a cutoff at about 1.9×10^{26} cm^{-5} of the emission measure of cool component and at about 2.6×10^{26} cm^{-5} of hot component. Inspection of the images shows that the values at the lower cutoff occur in coronal holes. This cutoff implies that even in coronal holes there is a lower limit to the amount of plasma present in the corona. This is not a sensitivity effect since the emission measure deduced in regions above the limb can be significantly less than this cutoff. Further, we believe that it is unlikely to be due to the wings of the telescope point-spread function since measurements show that the spatial response drops to 2×10^{-5} over a distance of 20 pixels, and there were no very bright active regions that might produce significant contamination of distant coronal holes. In quiet-Sun regions we find an average value for the emission measure of about 1.0×10^{27} cm^{-5} for the cool component and about 1.5×10^{27} cm^{-5} for the hot component. We have looked at many EIT data sets over a period over 2 years (1996–1998) and find that such cutoffs and average values in the emission measure distribution on the disk are always present, although they may vary on long timescales by a factor of 3. However, such variation is difficult to disentangle from gain variations in the telescope at this stage, and we caution that this result needs to be confirmed when the calibration is better understood. Such changes in the global distribution of the amount of plasma present provide an important constraint for models of mass balance and transport in the corona, and if it does indeed vary over the solar cycle it would be an important finding.

We have also studied the correlation between the fitted quantities in our two–thermal-component model. We find no overall correlation between temperature and emission measure for either the cool or the hot component. Detailed inspection show that there exists a weak correlation (in the sense of higher temperature pixels having higher emission measures) for pixels with strong emission, e.g., in active regions and bright points. Yoshida & Tsuneta (1996) also found that there was no correlation between temperature and emission measure in their study of the temperature structure (>3 MK) of active regions based on SXT observations. This observational result is not consistent with the conventional view that coronal heating drives chromospheric evaporation and thus controls the emission measure present in the corona (e.g., Craig & McClymont 1986). The balance between heating and cooling may be complex in a dynamic corona. Similarly, there is no overall correlation between the temperatures of the cool and hot components in the same pixel. However, there is a strong correlation between the emission measure of the cool component and that of the hot component. Combined with the fact that the emission measure of the hot component is always larger than or equal to that of the cool component, this correlation suggests the action of a rapid-heating/slow-cooling process in the corona. In a future paper, we will investigate these phenomena by looking at trends in the behavior of the statistical properties of active regions, coronal loops, quiet Sun, filament channels, coronal holes, and bright points for a long period of EIT data.

Finally, we point out one striking counter-intuitive feature of the T_H map of Figure 7: the polar coronal holes appear bright, i.e., they are hotter than the quiet Sun. This is unexpected since it is well known that coronal holes are dominated by cool plasma. We will explain the source of this anomaly in the following section.

5. ANOMALOUS SOLUTIONS IN CORONAL HOLES

In our two-component solutions, the temperature of the hot component in coronal holes (typically 2.0 MK) is found to be higher than that in quiet-Sun regions (1.9 MK), and the associated emission measure of the hot component in coronal holes (typically 6×10^{26} cm^{-5}) is also somewhat higher than that in quiet-Sun regions (5×10^{26} cm^{-5}). This anomaly of the two-temperature solutions in coronal holes is apparent in Figure 6, in which the hot-component solution for the dark quiet-Sun and coronal hole model DEMs deviate significantly from the predicted values. Thus, the unusually high-temperature solution found in coronal hole is not realistic. Based on SXT observations requiring careful background subtraction and using an isothermal assumption, Hara et al. (1996) also reported high temperatures in coronal holes: temperatures of 1.8–2.4 MK with emission measures of 3×10^{25}–2×10^{26} cm^{-5}. While there may be some hot material in coronal holes, we do not believe that our solution is finding the material reported by Hara et al. (1996). Rather, we believe that the anomaly in our solution is caused by the blend of very cool Mg VII/Si VII lines ($\sim$0.63 MK) with hot Fe XV lines ($\sim$2.1 MK) within the EIT 284 Å bandpass. This blend is also responsible for the low-level intranetwork structures seen in the EIT 284 Å images. The observed flux in the EIT 284 Å image is usually dominated by the emission from hot plasma producing strong Fe XV lines, since the primary (hot) peak of the normalized response dominates the secondary (cool) peak in height and width (as seen in Fig. 1). However, in coronal holes where very little material at 2 MK (or hotter) is present, a significant amount of cool plasma (<1.0 MK) can be responsible for a large fraction of the observed EIT 284 Å flux. We illustrate this argument in Figure 9, in which we plot the temperature response curves for the EIT 284 Å bandpass weighted by the four CHIANTI DEMs discussed before (i.e., the curves show the relative contribution to the observed flux of different temperatures given the distribu-

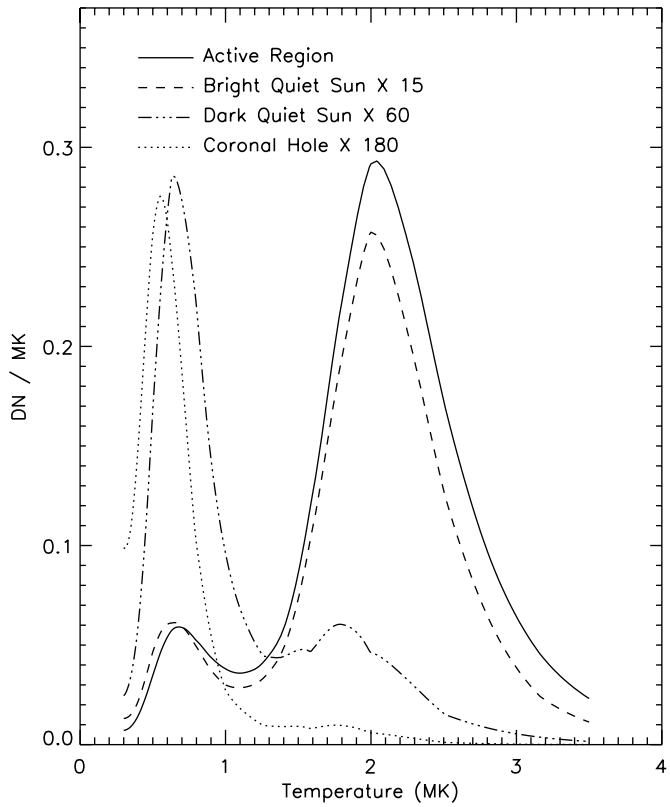

FIG. 9.—DEM-weighted temperature response curves for the EIT 284 Å bandpass. The four input model DEMs are the CHIANTI active-region, bright quiet-Sun, dark quiet-Sun, and coronal hole DEMs, respectively. The curves have been scaled as shown in the labels in order to better view the curves.

tion of emission measure with temperature specified by each DEM). Clearly, in the cases of the active-region and bright quiet-Sun DEMs, the EIT 284 Å flux is dominated by the hot Fe XV lines, but in the cases of the dark quiet-Sun and coronal hole DEMs, the flux from the cool Mg/Si lines dominates. Quantitatively, the fraction of the EIT 284 Å flux contributed by plasma with temperature less than 1 MK is about 9%, 12%, 60%, and 90% for the above four CHIANTI model DEMs, respectively. In our algorithm, since the contribution to EIT 284 Å bandpass from the very cool plasma (through the secondary peak) is attributed instead to hot material (still treated as in the primary peak) and there is no corresponding contribution to the EIT 195 Å image, the inferred temperature and emission measure of the hot component in coronal holes appear to be relatively higher than they really are.

One can think of two methods to deal with this anomaly. The first is to subtract the contribution of the cool Mg/Si lines from the observed EIT 284 Å flux before proceeding with the two-temperature analysis. The second is to search for the two thermal components over a different temperature range. We are still restricted by the fact that we measure only three numbers at each pixel, and therefore cannot invoke a model that has more than three free parameters. For this reason we cannot simply add an additional component to account for the cool material. Instead, in order to carry out a subtraction we must assume a fixed relationship of the emission measure in this temperature range to that in a measured range. We have investigated this relationship for a range of model DEMs consisting of a single-Gaussian component whose peak temperature varies from 0.5 to 3.0 MK and whose width varies from 0 MK (isothermal) to 5 MK (evenly distributed plasma). For a given DEM, it is easy to calculate the predicted flux in each bandpass, and specifically the percentage of the Mg/Si line contribution to the EIT 284 Å bandpass. Plotting this percentage against the EIT 195 Å/171 Å ratio for a wide range of these Gaussian DEMs, we find a coarse correlation: the smaller the EIT 195 Å/171 Å ratio (i.e., the cooler the cool component), the larger the percentage contribution to the EIT 284 Å bandpass from the cool lines. Using typical EIT 195 Å/171 Å ratios from Figure 3 for different regions of the solar atmosphere, we predict on the basis of this correlation that less than 5% of the EIT 284 Å flux in active regions comes from the Mg/Si lines, less than 10% in diffuse regions, and less than 20% in quiet-sun regions. However, in coronal holes more than 40% of the EIT 284 Å flux may come from the cool lines.

Interestingly, using a single-Gaussian DEM with varying peak temperature and width we can successfully reproduce the observed ratios for all the regions of the ratio plane in Figure 3 that are occupied by the data points except for region A, which corresponds to coronal holes. There is no single-Gaussian DEM that can reproduce the high EIT 284 Å/195 Å ratio (>0.04) while simultaneously producing a low EIT 195 Å/171 Å ratio (<0.5). We therefore argue that coronal holes may have a DEM distribution rather different from other coronal regions. One possible distribution that reproduces these ratios is the combination of a narrow and very cool component (e.g., a Gaussian with a peak at 0.6 MK and width less than 0.3 MK) with a hot but broad component (e.g., a Gaussian with a peak at 0.9 MK and width 1.0 MK). If such a DEM is appropriate to coronal holes, it suggests that more than 70% of the EIT 284 Å flux in coronal holes is due to the Mg/Si lines.

The alternative approach to this anomaly is to process the input EIT images by separating coronal holes from other regions. In regions where the normal procedure finds a high T_H in regions of low EM_C, we can search for two components in the range 0.4–1.7 MK rather than 0.8–2.7 MK. In this approach, we totally ignore the flux contribution from hot Fe XV lines in the EIT 284 Å bandpass. However, we find that there are no pairs of temperatures in this range for which solutions exist in any region of the ratio plane (Fig. 3) that is observed to be occupied by actual data, including region A, which contains the coronal hole points. Solutions exist only for very small ratios of EIT 195 Å/EIT 171 Å (<0.25) where no data points occur.

We therefore emphasize that care must be taken in interpreting the EIT 284 Å images: in regions where little hot material is present, they can be dominated by material that is actually much cooler than the typical quiet-Sun corona.

6. DISCUSSION AND CONCLUSION

Any quantitative analysis of EIT images must necessarily produce an approximation to the true DEM in the temperature range to which EIT's coronal images are sensitive, primarily 0.7–2.8 MK. In this paper, we have presented a modified image-ratio method whereby we approximate the coronal DEM by two thermal components. The products of the algorithm are full-resolution temperature and emission measure maps of the Sun's corona in two temperature regimes: one 0.8–1.6 MK, the other 1.6–2.6 MK. We have

shown that isothermal models based on pairs of EIT images provide a poor representation of the plasma to which EIT is sensitive. The method we have developed will be made available as part of the EIT software package. It imposes a minimum temperature ratio constraint that effectively minimizes the total emission measure in order to determine a solution for the four parameters needed to describe such a model from the three measured fluxes in each EIT pixel. We have demonstrated that the two thermal components produced by this technique do indeed provide a good match to model DEMs typical of the solar atmosphere. This method complements the approach of fitting parameterized functional forms of the DEM being pursued by Cook et al. (1998). The temperature ratio between the two components is a reflection of the broadness of the actual DEM distribution of the plasma. The difference of the emission measure between the two components reveals the slope of the DEM, which may be dependent on the level of heating. The two-component model could also be simply reduced to an isothermal model: the sum of the two emission measures of the hot and cool components from our solution should be close to the total emission measure of the DEM in the relevant temperature range, while the average of the two temperatures weighted by the two emission measures should be close to the average temperature of the DEM. Given the uncertainty in instrument calibration and atomic data as well as the fact that we are approximating a complicated DEM with a simple model, the temperature and emission measure maps derived will not be suitable for many detailed quantitative purposes, for which, e.g., specific CDS studies will be preferred. However, the two-temperature EIT models should be adequate for many general studies where relative comparisons between coronal features rather than absolute quantities are desired, and for studies of global properties such as energetics.

The preliminary results of our two–thermal-component model show that the appearance of the observed flux images is mostly a manifestation of the emission measure distribution in the corona, while temperature maps can emphasize fine-scale structure, which is less visible in the flux images. We also find that there exists a firm lower limit for the emission measure distributions of both hot and cool components on the disk. There is no overall correlation between temperature and emission measure for either component, and no overall correlation between cool and hot temperatures at the same pixel. However, there is strong correlation between the emission measure of the cool component and that of the hot component. The emission measure of the hot component is always found to be at least as large as that of the cool component, meaning that single-temperature models based on the 195 Å/171 Å ratio probably miss most of the coronal plasma to which EIT is sensitive. A statistical study of the properties of different coronal features will be pursued later.

In general, our method provides a consistent way to diagnose the temperature and emission measure of structures of the Sun's corona in EIT's range of sensitivity from 0.7 to 2.8 MK. This temperature regime is uniquely interesting since the bulk of the coronal DEM resides there: only in very active regions does the peak of the DEM lie outside this range. The temperature maps resulting from this technique have rather low noise because of the excellent sensitivity of EIT, and thus can be used to study the detailed temperature distribution of both fine and large coronal structures. In addition, it is a trivial matter to extend this technique to TRACE data sets consisting of bandpasses centered at 171, 195, and 284 Å: all that needs to be changed are the temperature response functions.

There are some limitations to our two–thermal-component model (apart from the fact that it is just a representation of the true DEM) that are mainly imposed by the nature of the data but which must be borne in mind. First, the diagnostic is limited to the temperature regime 0.7 to 2.8 MK. In active regions where a significant amount of plasma may exceed 3.0 MK, the EIT simply does not "see" the very hot plasma. The addition of SXT data is desirable for such active regions (e.g., see Yoshida & Tsuneta 1996). Secondly, the blend of very cool Mg/Si lines with hot Fe XV lines in the EIT 284 Å bandpass induces a false solution for the hot component in coronal holes. Special care is required to remove the effect of this blend, such as subtracting the Mg/Si line contribution based on a correlation with the EIT 195 Å/171 Å ratio. This approach is available as an option in the code, but we recommend against using it for quantitative results at this stage because the resulting models still appear to be unsatisfactory in coronal holes. We plan to investigate this discrepancy further in the future.

The technique presented is very suitable to study heating and cooling processes in large-scale structures in the corona. Such studies have not really been possible since the days of *Skylab*, but EIT offers ideal temporal and spatial coverage for such a study. The statistical behavior of the temperature, emission measure, pressure, and energetics of large-scale structures such as active regions, diffuse regions, quiet regions, filament channels, and coronal holes is important for understanding the overall structure of the Sun's atmosphere. In a future publication, we also plan to compare radio images calculated from the temperature and emission measure maps from the two–thermal-component model with the actually observed radio images, in order to reconcile the radio observations of the solar corona with the X-ray and EUV observations. In addition, daily coronal pressure maps may prove to be valuable as a boundary condition for real–time simulations of solar wind behavior in the heliosphere.

We thank the referee John Cook for his thoughtful comments, which led to significant improvements in the paper. This research was supported by NASA grants NAG 5-6257 and NAG 5-7901, and NSF grant ATM 96-12738. We thank Jeff Newmark for extensive help and advice, and Dan Moses, John Cook, Jim Klimchuck, Stuart Vogel, Alexander Nindos, and Markus Aschwanden for valuable discussions.

REFERENCES

Arnaud, M., & Raymond, J. 1992, ApJ, 398, 394
Aschwanden, M. J., Newmark, J. S., Delaboudiniere, J.-P., Neupert, W. M., Klimchuk, J. A., Gary, G. A., Portier-Fozzani, F., & Zucker, A. 1998, in Proc. CESRA Workshop on Coronal Explosive Events, ed. S. Pohjolainen (Helsinki: Metsaehovi Radio Research Station), 19
Benz, A. O., & Krucker, S., 1999, A&A, 341, 286
Brosius, J. W., Davila, J. M., Thomas, R. J., & Monsignori-Fossi, B. C. 1996, ApJS, 106, 143
Cook, J. W., Newmark, J. S., Moses, J. D., Defise, J. M., & Auchere, F. 1998, EOS, 79,17, S290
Craig, I. J. D., & McClymont, A. N. 1986, ApJ, 307, 367
Delaboudinière, J.-P., et al. 1995, Sol. Phys., 162, 291

Dere, K. P. 1982, Sol. Phys., 77, 77
Dere, K. P., Landi, E., Mason, H. E., Monsignori Fossi, B. C., & Young, P. R. 1997, A&AS, 125, 149
Dere, K. P., & Mason, H. E. 1993, Sol. Phys., 144, 217
Dupree, A. K. 1972, ApJ, 178, 527
Dupree, A. K., Huber, M. C. E., Noyes, R. W., Reeves, W. H., & Withbroe, G. L. 1973, ApJ, 182, 321
Griffiths, N. W., & Jordan, C. 1998, ApJ, 497, 883
Hara, H., Tsuneta, S., Acton, L. W., Bruner, M. E., Lemen, J. R., & Ogawara, Y. 1996, Adv. Space Res., 17, 4
Heroux, L., & Higgins, J. E. 1977, J. Geophys. Res., 82, 3307
Mason, H. E., Young, P. R., Pike, C. D., Harrison, R. A., Fludra, A., Bromage, B. J. I., & Del Zanna, G. 1997, Sol. Phys., 170, 143
McIntosh, S. W., Brown, J. C., & Judge, P. G. 1998, A&A, 333, 333
Meyer, J.-P. 1985, ApJS, 57, 173
Moses, D., et al. 1997, Sol. Phys., 175, 571
Neupert, W. M., et al. 1997, AAS/SPD meeting, 29, 1.15
Nitta, N., & Yaji, K., 1997, ApJ, 484, 927
Raymond, J. C., & Doyle, J. G. 1981, ApJ, 247, 686
Tsuneta, S. 1999, in PASP Conf. Ser., Proc. High-Resolution Solar Atmospheric Dynamics Workshop, ed. J. Bookbinder & E. DeLuca (San Francisco: ASP), in press
Tsuneta, S., et al. 1991, Sol. Phys., 136, 37
Vernazza, J. E., & Reeves, E. M. 1978, ApJS, 37, 485
Yoshida, T., & Tsuneta, S. 1996, ApJ, 459, 342